Revision 1

Xuite, $Ca_3Fe_2[(Al,Fe)O_3(OH)]_3$, a new mineral of the garnet group: Implications for wide occurrence of nano-minerals

Seungyeol Lee[1,2,3,*] and Xiaofeng Guo[4,5]

[1]Department of Geoscience, University of Wisconsin–Madison, Madison, WI 53706, USA

[2]USRA Lunar and Planetary Institute, 3600 Bay Area Boulevard, Houston, TX 77058, USA

[3]ARES, NASA Johnson Space Center, 2101 NASA Parkway, Houston, TX 77058, USA

[4]Department of Chemistry, Washington State University, Pullman, WA 99164, USA

[5]Alexandra Navrotsky Institute for Experimental Thermodynamics, Washington State University, Pullman, WA 99164, USA

* Corresponding author:

Dr. Seungyeol Lee

Tel: 1-608-770-9310

Email: slee2@lpi.usra.edu

ABSTRACT

Xuite, $Ca_3Fe_2[(Al,Fe)O_3(OH)]_3$, is a new member of the garnet supergroup discovered in basaltic scoria from Menan Volcanic Complex, Idaho, USA. Oxidation of Fe-bearing pyroclasts at high temperatures led to the formation of xuite, together with luogufengite, valleyite, and hematite inside the silicate glass matrix. The measured crystal size of xuite ranges from ~200 to 800 nm. The empirical chemical formula of xuite is $(Ca_{0.92}Mg_{0.08})_3(Fe_{0.96}Ti_{0.04})_2[(AlO_4H)_{0.44}(FeO_4H)_{0.33}(SiO_4)_{0.05}(\square O_4H_4)_{0.18}]_3$. Xuite has a space group of $Ia\bar{3}d$; its unit-cell parameter refined from high-resolution synchrotron X-ray diffraction (XRD) data is a = 12.5056(5) Å, and Z = 8 (calculated density = 3.53 g/cm^3). Fourier-transform infrared spectroscopy spectrum of xuite shows absorption bands at 3682 and 3579 cm^{-1}, indicating the presence of OH^- in the hydrogarnet structure. *In-situ* high-temperature synchrotron XRD combined with thermogravimetry and differential scanning calorimetry reveals that xuite undergoes dehydroxylation to form brownmillerite (Ca_2FeAlO_5) from ~236 to ~396 °C. Xuite occurs in the form of nano-crystals with a soft magnetic property, which provides important insights into the origin of basaltic scoria and associated paleomagnetism. Xuite was also found in Wyoming paralava, suggesting the possibility of its wide-occurrence in various geological environments. The mineral was named after Huifang Xu and Hongwu Xu in honor of their sustained contributions to minerals science.

Keywords: xuite, garnet group, luogufengite, valleyite, synchrotron X-ray diffraction, transmission electron microscopy

INTRODUCTION

The new mineral xuite, a magnetic ferric iron-rich hydrogarnet phase $Ca_3Fe_2[(Al,Fe)O_3(OH)]_3$, was discovered on vesicles' surfaces of basaltic scoria from Menan volcanic Complex, Idaho, USA. Formation of scoria was due to rapid vesiculation during the explosive eruption of tholeiitic basalts (Russell and Brisbin 1990). Oxidation of Fe-bearing pyroclasts at high temperatures led to the formation of xuite, together with luogufengite (IMA2016-005), valleyite (IMA2017-026), maghemite, hematite, and quartz (Xu et al. 2017; Lee et al. 2019). Xuite is a new member of hydrogarnet subgroup in the garnet supergroup, according to the current garnet classification (Grew et al. 2013).

This paper presents the crystal structure, chemical composition, mineral association, and dehydration process of xuite. The xuite phase was identified using high-resolution synchrotron X-ray diffraction (XRD) and transmission electron microscopy (TEM), which yielded the crystal structural and chemical information. Rietveld refinement and Fourier-transform infrared spectroscopy (FTIR) confirmed the existence of OH^- in the structure. *In-situ* high-temperature synchrotron XRD combined with thermogravimetric analysis (TGA) and differential scanning calorimetry (DSC) revealed the decomposition of xuite on heating. The mineral name has been approved by the Commission on New Minerals, Nomenclature and Classification (CNMNC) of the International Mineralogical Association (IMA 2018-135a) (Lee and Guo 2021). The mineral was named after Huifang Xu of the University of Wisconsin – Madison, USA, and Hongwu Xu of the Los Alamos National Laboratory, USA, in honor of their sustained contributions to minerals research, including the discovery of two other Fe-bearing nano-minerals associated with xuite: luogufengite and valleyite. Xuite has been deposited in the collection of Geology Museum of the

Department of Geoscience, the University of Wisconsin-Madison, with specimen numbers UWGM 2341, UW2342, and UWGM 2343.

SAMPLES AND METHODS

The samples were carefully scratched off from the vesicles' surfaces of the collected basaltic scoria (Supplementary Fig. S1). These powder samples were placed in a 10M NaOH solution at 80 °C for 2 days to remove silicate glass following previously described procedures (Lee and Xu 2016a; Xu et al. 2017; Lee and Xu 2018). After washing the powders with distilled water several times, xuite was enriched using a magnetic bar to minimize portions of non-magnetic minerals because it has soft magnetic properties. The xuite was further enriched by removing permanently magnetized crystals such as luogufengite and valleyite by picking them up with an iron needle from pre-magnetized samples. These magnetic enrichment steps were repeated several times.

High-resolution synchrotron XRD data were collected at beamline 11-BM of the Advanced Photon Source (APS) at Argonne National Laboratory. XRD patterns were recorded using a wavelength (λ) of 0.414231 Å, as calibrated using a LaB_6 standard. Finely ground powders of the samples were placed in polyimide tubes with an inner diameter of 0.8 mm. The crystal structure of xuite and the ratios of mineral phases present in the sample were determined by the Rietveld method using the TOPAS 5 software (Rietveld 2014). *In-situ* high-temperature synchrotron XRD data were collected at beamline 28-ID-2 of National Synchrotron Light Source II (NSLS II) at Brookhaven National Laboratory. The wavelength of the X-ray beam was 0.237 Å and its size was 0.60×0.20 mm. Finely ground powders of a xuite-bearing sample were contained in a silica glass capillary (1 mm ID, 0.25 mm thickness). The capillary was then inserted into a quadrupole lamp

furnace for *in-situ* heating XRD measurements. The sample temperature was calibrated by measuring the coefficient of thermal expansion of a standard ceria powder at various temperature points with a heating rate of ~20 °C /min. The sample was heated from room temperature up to 1000 °C to examine the dehydroxylation process of xuite.

Bright-field and high-resolution TEM images as well as selected-area electron diffraction (SAED) patterns were obtained using a Philips CM200-UT microscope operated at 200 kV. TEM specimens were prepared by depositing a suspension of the enriched samples on a lacy carbon-coated Cu grid. Chemical composition was obtained using a TEM-EDS system equipped with a Li-drifted Si detector. An electron beam diameter of ~50 nm was used to collect X-ray EDS spectra with fayalite, anorthite, and forsterite as the standards to quantify the element fractions of Fe, Ca, Al, Mg, and Si in the samples (Supplementary Table. S1).

FTIR spectrum of a xuite-bearing sample was collected in the mid-infrared range, 3800–3200 cm^{-1}. The sample was preheated at 110°C under vacuum for 12 hours to remove adsorbed water. The infrared spectrum was recorded using a Nicolet Magna 860 Fourier transform spectrometer (Thermo-Nicolet, Madison, WI) with a resolution of 4 cm^{-1} with 64 scans co-added and an aperture setting of 10 μm × 10 μm. Thermogravimetry (TG) and differential scanning calorimetry (DSC) were conducted on a Netzsch STA 449F1 analyzer. The curves were obtained in a temperature range from 25 to 800 °C with a heating rate of 10°C/min under a flowing Ar gas (20 mL/min).

RESULTS AND DISCUSSION

High-resolution synchrotron XRD pattern of a sample treated by magnetic enrichment steps reveals the occurrence of xuite, together with luogufengite, hematite, quartz, and calcite (Figs.

1 and 2). Diffraction peaks of xuite are listed in Table 1. The (112), (022), (004), (024), (224), (116) and (235) peaks of xuite do not overlap with those from the coexisting minerals, facilitating its discovery (Fig. 1). Two zoomed-in areas of the XRD pattern show that the (224) peak of xuite is sharper than the peaks from nanophase luogufengite (Fig. 2). Rietveld analysis yielded the following estimates of mean crystallite sizes: xuite (454 nm), luogufengite (39 nm), and hematite (108 nm) based on their Bragg peaks' widths.

Figures 3 and 4 show bright field TEM images, SAED, and high-resolution TEM images of xuite nano-crystals. The size of xuite crystals ranges from ~200 to ~800 nm. High-resolution TEM images and SAED patterns confirm that xuite has a cubic symmetry with crystallographic forms of {110} (Figs. 3 and 4). Compositional analyses were performed using X-ray EDS under TEM (a beam size of ~50 nm in diameter) with k-factors determined using mineral standards under the same experimental condition (Fig. 5) (Cliff and Lorimer 1975). The obtained oxide contents (wt.%) from 6 analyses of separate xuite crystals are reported in Table 2. From these results, the empirical formula of xuite is derived to be $(Ca_{0.92}Mg_{0.08})_3(Fe_{0.96}Ti_{0.04})_2[(AlO_4H)_{0.44}(FeO_4H)_{0.34}(SiO_4)_{0.05}(O_4H_4)_{0.17}]_3$.

The crystal structure of xuite was determined based on an input model of the garnet structure of Armbruster and Geiger (1993) using the Rietveld method combined with TEM-EDS results. Positions of the cations were fixed at special positions, as defined by the cubic symmetry (space group $Ia\bar{3}d$). Fractional coordinates, occupancies, and isotropic displacement parameters of all atoms from the refined xuite structure are listed in Table S2. Rietveld refinement suggests that xuite is a hydrogarnet phase that contains (Ca, Mg) in the *X*-site, (Fe, Ti) in the octahedral *Y*-site, and (Al, Fe, Si) and hydroxyl ($\square O_4H_4$) in the tetrahedral *Z*-site (Fig. 6). Occupancies of cation sites from Rietveld analysis of powder synchrotron XRD data suggest about 7.7 wt.% of OH^- in the

131 xuite structure following the charge neutrality requirement (Table S2), which is consistent with the
132 corresponding amount of H_2O calculated based on garnet stoichiometry and charge balance from
133 TEM-EDS (Table 2). The hydrogen position is adopted from another OH-bearing garnet phase
134 (katoite) (Ferro et al. 2003). The bond distances of the refined xuite structure are in excellent
135 agreement with those of other garnet phases (Armbruster and Geiger 1993; Rodehorst et al. 2002;
136 Grew et al. 2013) (Table 3).

137 Xuite, $Ca_3Fe_2[(Al,Fe)O_3(OH)]_3$, is a new member of the garnet supergroup and of the
138 hydrogarnet subgroup. According to the garnet formula of $X_3Y_2Z_3\phi_{12}$ (ϕ=O+OH), the structure
139 contains Ca in the *X*-site, Fe in the octahedral *Y*-site, and $(Al,Fe)O_4H$ in the tetrahedral *Z*-site.
140 Similarly, katoite, $Ca_3Al_2(OH)_{12}$, contains Ca in the *X*-site, Al in the *Y*-site, and vacancy in *Z*-site
141 (Lager et al. 2005). Bitikleite, $Ca_3(SbSn)(AlO_4)_3$, and usturite, $Ca_3(SbZr)(FeO_4)_3$, are dominated
142 by Al and Fe, respectively, over their *Z*-sites, although their *Y*-sites are occupied by (SbSn) and
143 (SbZr), instead of Fe_2 (Galuskina et al. 2010; Grew et al. 2013). Schorlomite, $Ca_3Ti_2(SiFe^{3+}_2)O_{12}$,
144 contains Si and Fe^{3+} in its *Z*-site and Ca and Ti^{4+} in the *X*-site and *Y*-site, respectively
145 (Chakhmouradian and McCammon 2005).

146 The FTIR spectrum of a xuite-bearing sample (after its surface water was removed) shows
147 absorption bands at 3682 and 3579 cm^{-1}, which are similar to those of hydrogarnet, katoite
148 $[Ca_3Al_2(SiO_4)_{1.5}(OH)_6]$ (Rossman and Aines 1991), confirming the presence of OH^- in the xuite
149 structure (Fig. 7). Other phases in the samples, i.e., luogufengite, hematite, quartz, and calcite, are
150 all anhydrous. The broadness of the bands can be attributed to varying strengths of the OH bonds
151 that are associated with AlO_4H, FeO_4H and $(OH)_4$ in the structure (Fig. 7a).

152 *In-situ* high-temperature synchrotron XRD reveals that xuite underwent decomposition
153 (dehydroxylation) to form brownmillerite $[Ca_2(Fe,Al)_2O_5]$ and hematite in the temperature range

236–396 °C (Fig. 8). The lattice parameters of brownmillerite suggest the Ca_2FeAlO_5 composition (Rodehorst et al. 2002), which is consistent with the xuite composition, $Ca_3Fe_2[(Al,Fe)O_3(OH)]_3$. The dehydroxylation reaction can be simplified as: $2Ca_3Fe_2[(Al_{0.5},Fe_{0.5})O_3(OH)]_3$ (Xuite) → $3Ca_2FeAlO_5$ (Brownmillerite) + $2Fe_2O_3$ (Hematite) + $3H_2O$ (gas). TG and DSC analysis also confirmed the dehydration of xuite from ~ 230 to ~395 °C (Fig. 9). TG indicates a ~0.8 % weight loss during the decomposition of xuite (Fig. 9). Considering the content of xuite in the sample (9.4 wt.%) (Fig. 1) and the amount of H_2O (7.6 wt.%) (Table 2), the value of weight loss (~0.8 %) is reasonably consistent with the water content of xuite. The continuous mass loss up to ~700 °C shown in the TG curve (Fig. 9) may be attributed to the removal of surface hydroxyl from the coexisting luogufengite and hematite nanoparticles. Similar behavior has been observed in synthetic Fe_2O_3 nanoparticles (Lassoued et al. 2017).

IMPLICATIONS

Nano-minerals play essential roles in many geochemical processes involving adsorption and transport of ions, redox reactions, metabolic processes, and global cycles of elements (Hochella et al. 2008; Lee et al. 2016; Lee and Xu 2016b). However, detailed studies of nano-minerals have been challenging because of their nanocrystalline nature and coexistence with other minerals (Hotze et al. 2010; Lee and Xu 2020; Lee et al. 2021). We have integrated high-resolution synchrotron XRD with high-resolution TEM to study nano-minerals and have discovered new minerals of xuite, together with luogufengite and valleyite from Menan volcanic complex, Idaho (Xu et al. 2002; Xu et al. 2014; Xu et al. 2017; Lee et al. 2019). More recently, we found xuite in Wyoming paralava (Supplementary Fig. S1). This second discovery indicates potential wide-occurrence of this new mineral in a variety of geological environments.

177 This study confirmed that the combined method of synchrotron XRD and TEM is a
178 powerful tool for identifying nano-minerals. Especially, high-resolution synchrotron XRD allows
179 for clear separation of weak and broad diffraction peaks from nano-minerals, which cannot be
180 resolved or detected by conventional XRD. In addition, direct imaging and analysis by HRTEM
181 coupled with SAED and X-ray EDS analysis can determine the structure and chemistry at the
182 nanoscale. We expect this integrated approach will lead to the discovery of many other new nano-
183 minerals in the future.
184
185 **ACKNOWLEDGMENTS**
186 The authors thank Dr. Michael Hochella and an anonymous reviewer for their helpful
187 comments. High-resolution XRD was carried out at the Advanced Photon Source (beamline 11-
188 BM), Argonne National Laboratory, supported by the U. S. Department of Energy, Office of
189 Science, Office of Basic Energy Sciences under Contract No. DE-AC02-06CH11357. This
190 research also used resources at beamline 28-ID-2 of the National Synchrotron Light Source II, a
191 U.S. Department of Energy (DOE) Office of Science User Facility operated for the DOE Office of
192 Science by Brookhaven National Laboratory under Contract No. DE-SC0012704. The authors
193 gratefully acknowledge use of facilities and instrumentation supported by NSF through the
194 University of Wisconsin Materials Research Science and Engineering Center (DMR-1720415).
195 We are grateful to Huifang Xu and Hongwu Xu for their continuous guidance and support over the
196 years.
197

REFERENCES

Armbruster, T., and Geiger, C.A. (1993) Andradite crystal chemistry, dynamic X-site disorder and structural strain in silicate garnets. European Journal of Mineralogy, 5(1), 59-71.

Chakhmouradian, A., and McCammon, C. (2005) Schorlomite: a discussion of the crystal chemistry, formula, and inter-species boundaries. Physics and Chemistry of Minerals, 32(4), 277-289.

Cliff, G., and Lorimer, G.W. (1975) The quantitative analysis of thin specimens. Journal of Microscopy, 103(2), 203-207.

Ferro, O., Galli, E., Papp, G., Quartieri, S., Szakáll, S., and Vezzalini, G. (2003) A new occurrence of katoite and re-examination of the hydrogrossular group. European Journal of Mineralogy, 15(2), 419-426.

Galuskina, I.O., Galuskin, E.V., Armbruster, T., Lazic, B., Dzierzanowski, P., Gazeev, V.M., Prusik, K., Pertsev, N.N., Winiarski, A., and Zadov, A.E. (2010) Bitikleite-(SnAl) and bitikleite-(ZrFe): new garnets from xenoliths of the Upper Chegem volcanic structure, Kabardino-Balkaria, Northern Caucasus, Russia. American Mineralogist, 95(7), 959-967.

Grew, E.S., Locock, A.J., Mills, S.J., Galuskina, I.O., Galuskin, E.V., and Hålenius, U. (2013) Nomenclature of the garnet supergroup. American Mineralogist, 98(4), 785-811.

Hochella, M.F., Lower, S.K., Maurice, P.A., Penn, R.L., Sahai, N., Sparks, D.L., and Twining, B.S. (2008) Nanominerals, mineral nanoparticles, and earth systems. science, 319(5870), 1631-1635.

Hotze, E.M., Phenrat, T., and Lowry, G.V. (2010) Nanoparticle aggregation: challenges to understanding transport and reactivity in the environment. Journal of environmental quality, 39(6), 1909-1924.

Lager, G.A., Marshall, W.G., Liu, Z., and Downs, R.T. (2005) Re-examination of the hydrogarnet structure at high pressure using neutron powder diffraction and infrared spectroscopy. American Mineralogist, 90(4), 639-644.

Lassoued, A., Dkhil, B., Gadri, A., and Ammar, S. (2017). Control of the shape and size of iron oxide (α-Fe_2O_3) nanoparticles synthesized through the chemical precipitation method. Results in physics, 7, 3007-3015

Lee, S., Shen, Z., and Xu, H. (2016) Study on nanophase iron oxyhydroxides in freshwater ferromanganese nodules from Green Bay, Lake Michigan, with implications for the adsorption of As and heavy metals. American Mineralogist, 101(9), 1986-1995.

Lee, S., and Xu, H. (2016a) Size-dependent phase map and phase transformation kinetics for nanometric iron (III) oxides ($\gamma \rightarrow \varepsilon \rightarrow \alpha$ pathway). The Journal of Physical Chemistry C, 120(24), 13316-13322.

-. (2016b) XRD and TEM studies on nanophase manganese oxides in freshwater ferromanganese nodules from Green Bay, Lake Michigan. Clays and Clay Minerals, 64(5), 523-536.

-. (2018) The role of ε-Fe_2O_3 nano-mineral and domains in enhancing magnetic coercivity: Implications for the natural remanent magnetization. Minerals, 8(3), 97.

-. (2020) Using complementary methods of synchrotron radiation powder diffraction and pair distribution function to refine crystal structures with high quality parameters—a review. Minerals, 10(2), 124.

Lee, S., Xu, H., Xu, H., Jacobs, R., and Morgan, D. (2019) Valleyite: A new magnetic mineral with the sodalite-type structure. American Mineralogist: Journal of Earth and Planetary Materials, 104(9), 1238-1245.

Lee S., and Guo, X. (2021) Xuite, IMA 2018-135a CNMNC Newsletter 59, Mineralogical Magazine, 85.

Lee, S., Xu, H., Xu, H., and Neuefeind, J. (2021) Crystal Structure of Moganite and Its Anisotropic Atomic Displacement Parameters Determined by Synchrotron X-ray Diffraction and X-ray/Neutron Pair Distribution Function Analyses. Minerals, 11(3), 272.

Rietveld, H.M. (2014) The rietveld method. Physica Scripta, 89(9), 098002.

Rodehorst, U., Geiger, C.A., and Armbruster, T. (2002) The crystal structures of grossular and spessartine between 100 and 600 K and the crystal chemistry of grossular-spessartine solid solutions. American Mineralogist, 87(4), 542-549.

Rossman, G.R., and Aines, R.D. (1991) The hydrous components in garnets: Grossular-hydrogrossular. American Mineralogist, 76(7-8), 1153-1164.

Russell, W., and Brisbin, W. (1990) Primary fractures within a tuff cone, North Menan Butte, Idaho, USA. Journal of volcanology and geothermal research, 40(1), 11-22.

Xu, H., Lee, S., and Xu, H. (2017) Luogufengite: A new nano-mineral of Fe2O3 polymorph with giant coercive field. American Mineralogist, 102(4), 711-719.

Xu, H., Navrotsky, A., Balmer, M.L., and Su, Y. (2002) Crystal Chemistry and Phase Transitions in Substituted Pollucites along the $CsAlSi_2O_6$-$CsTiSi_2O_{6.5}$ Join: A Powder Synchrotron X-ray Diffractometry Study. Journal of the American Ceramic Society, 85(5), 1235-1242.

Xu, H., Shen, Z., and Konishi, H. (2014) Si-magnetite nano-precipitates in silician magnetite from banded iron formation: Z-contrast imaging and ab initio study. American Mineralogist, 99(11-12), 2196-2202.

Figure Captions

Figure 1. Synchrotron XRD pattern (experimental and calculated XRD profiles overlapped as black and red lines, respectively) of the scoria sample shows diffraction peaks from xuite, luogufengite, hematite, quartz, and calcite. The differences between measured and calculated profiles are plotted below the XRD pattern. Percentages of individual mineral phases in the sample were calculated using the Rietveld method. Note that, to obtain the high-quality data, volcanic glass had been removed by dissolving it in a 10M NaOH solution at 80 °C for 2 days.

Figure 2. Two zoomed-in areas from the XRD pattern in Figure 1, showing the (224) and (246) peaks of xuite. The crystal sizes of phases affect the widths of their diffraction peaks. The peaks from quartz (Q) are much sharper than those from nanocrystalline xuite (X) (average size: 450 nm) and luogufengite (L) (average size: 40 nm).

Figure 3. (A) Bright-field TEM image showing a xuite crystal along the [001] direction. (B) A [001] zone-axis selected-area electron diffraction (SAED) pattern of the xuite crystal in Fig 3A. (C) A [$\bar{1}$10] zone-axis SAED pattern of xuite. (D) Bright-field TEM image showing a xuite crystal along the [$\bar{1}$11] zone-axis direction. (E) A [$\bar{1}$11] zone-axis SAED pattern of the xuite crystal in Fig 3D. (F) A [$\bar{1}$12] zone-axis SAED pattern of xuite.

Figure 4. High-resolution TEM images of xuite crystals along the *c*-axis (A) and the [$\bar{1}$11] zone-axis (B). Inserted at the up-right corners are Fast Fourier transform (FFT) patterns from the images.

Figure 5. Representative X-ray EDS spectra of xuite nano-crystals. C and Cu peaks are from the holey carbon-coated Cu grid that holds the specimen.

Figure 6. Polyhedral models of the xuite structure porjected along: (A) the [100]-zone-axis; and (B) the [111]-zone-axis. Brown octahedron = Fe,Ti; Blue tetrahedron = (Al,Fe,Si,□); Green ball = Ca; Orange sector = Mg; Red ball = O. The structure models were drawn using the Vesta software.

Figure 7. FTIR spectrum of the scoria xuite-bearing sample (after its surface water was removed)

294 shows absorption bands at 3682 and 3579 cm^{-1} (a), which are similar to those of katoite
295 $[Ca_3Al_2(SiO_4)_{1.5}(OH)_6]$ (b) (Rossman and Aines, 1991), confirming the presence of OH^- in the
296 xuite structure. Other phases in the samples (luogufengite, hematite, quartz and calcite) are all
297 anhydrous. The broadness of the bands can be attributed to varying strengths of the OH bonds that
298 are associated with AlO_4H, FeO_4H and $(OH)_4$ in the structure.
299
300 **Figure 8.** *In-situ* high-temperature synchrotron XRD patterns of a xuite-bearing sample (Idaho)
301 from 21 to 451 °C. Some un-overlapped diffraction peaks of xuite clearly show that the
302 decomposition of xuite starts from ~236 °C and ends at ~396 °C. Brownmillerite $[Ca_2(Fe^{3+},Al)O_5]$
303 appears as the dehydrated product. The lattice parameters of brownmillerite suggest the Ca_2FeAlO_5
304 composition (Redhammer et al. 2002). X = Xuite and Br = Brownmillerite.
305
306 **Figure 9.** Thermogravimetry (TG) and differential scanning calorimetry (DSC) curves of the
307 treated sample from Idaho scoria. There is a ~0.8 wt.% mass loss in the temperature range of xuite
308 decomposition. Since the content of xuite in the sample is 9.4 wt.% and the amount of H_2O is7.6
309 wt.%, the mass loss (~0.8 wt.%) is in good agreement with the chemical composition of xuite
310 inferred from EDS and structural analyses.

Table 1. Powder X-ray diffraction data of xuite.

d_{obs}	I_{obs}	d_{clac}	I_{clac}	*hkl*
5.1062	**15.7**	**5.1054**	**7.2**	**1 1 2**
4.4215	**65.4**	**4.4214**	**51.3**	**0 2 2**
3.3420	**24.0**	**3.3423**	**12.4**	**1 2 3**
3.1261	**62.5**	**3.1264**	**63.5**	**0 0 4**
2.7959	**100.0**	**2.7963**	**100.0**	**0 2 4**
2.6659	**15.2**	**2.6662**	**17.1**	**2 3 3**
2.5524	**63.1**	**2.5527**	**58.4**	**2 2 4**
2.2817	5.1	2.2832	3.3	1 2 5
2.0283	5.5	2.0287	4.3	2 3 5
		2.0287	0.9	1 1 6
1.8429	3.5	1.8439	5.3	1 3 6
1.7335	5.1	1.7342	8.3	0 4 6
1.6708	5.4	1.6711	8.5	2 4 6

Table 2. Chemical composition of xuite.

Analysis no.	1	2	3	4	5	6	Average
Fe_2O_3 (wt.%)	44.46	44.64	44.75	43.96	44.96	45.23	44.64
CaO	29.71	29.95	29.92	29.68	29.74	30.15	29.84
Al_2O_3	13.16	12.88	12.86	13.34	12.93	12.57	12.98
MgO	1.94	1.87	1.86	2.11	1.78	1.63	1.87
TiO_2	1.39	1.23	1.23	1.39	1.23	1.08	1.23
SiO_2	1.85	1.74	1.74	1.63	1.96	1.73	1.85
H_2O	7.49	7.69	7.64	7.89	7.40	7.61	7.59
Fe	2.89	2.90	2.91	2.84	2.93	2.94	2.90
Ca	2.75	2.77	2.76	2.73	2.76	2.79	2.76
Al	1.34	1.31	1.32	1.35	1.32	1.28	1.32
Mg	0.25	0.24	0.23	0.27	0.23	0.21	0.24
Ti	0.09	0.08	0.07	0.09	0.08	0.07	0.08
Si	0.16	0.15	0.16	0.14	0.17	0.15	0.16

Average chemical formula:
$(Ca_{0.92}Mg_{0.08})_3(Fe_{0.96}Ti_{0.04})_2((AlO_4H)_{0.44}(FeO_4H)_{0.34}(SiO_4)_{0.05}(O_4H_4)_{0.17})_3$

Notes: All calculations are based on 12 oxygen atoms of garnet structure. Hydrogen atoms are added for charge balance.

Table 3. Comparison of bond distances (Å) of xuite, bitikleite, andradite, grossular and katoite.

	X		Y_{OCT}		Z_{TET}		Reference
Xuite	Ca-O	2.501(8) x 4 2.438(8) x 4	Fe-O	2.018(10)	(Al,Fe,Si,□)-O	1.874(9)	This study
Bitikleite	Ca-O	2.555(3) x 4 2.408(3) x 4	(Sn,Ti)-O	2.040(3)	(Al,Fe)-O	1.807(3)	Galuskina et al. (2010)
Andradite	Ca-O	2.502(3) x 4 2.362(2) x 4	Fe-O	2.020(2)	Si-O	1.648(1)	Armbruster and Geiger, (1993)
Grossular	Ca-O	2.487(1) x 4 2.323(1) x 4	Al-O	1.928(1)	Si-O	1.645(1)	Rodehorst et al. (2002)
Katoite	Ca-O	2.522(1) x 4 2.449(1) x 4	Al-O	1.936(1)	□-O	1.932(1)	Lager et al. (2005)

Figure. 1

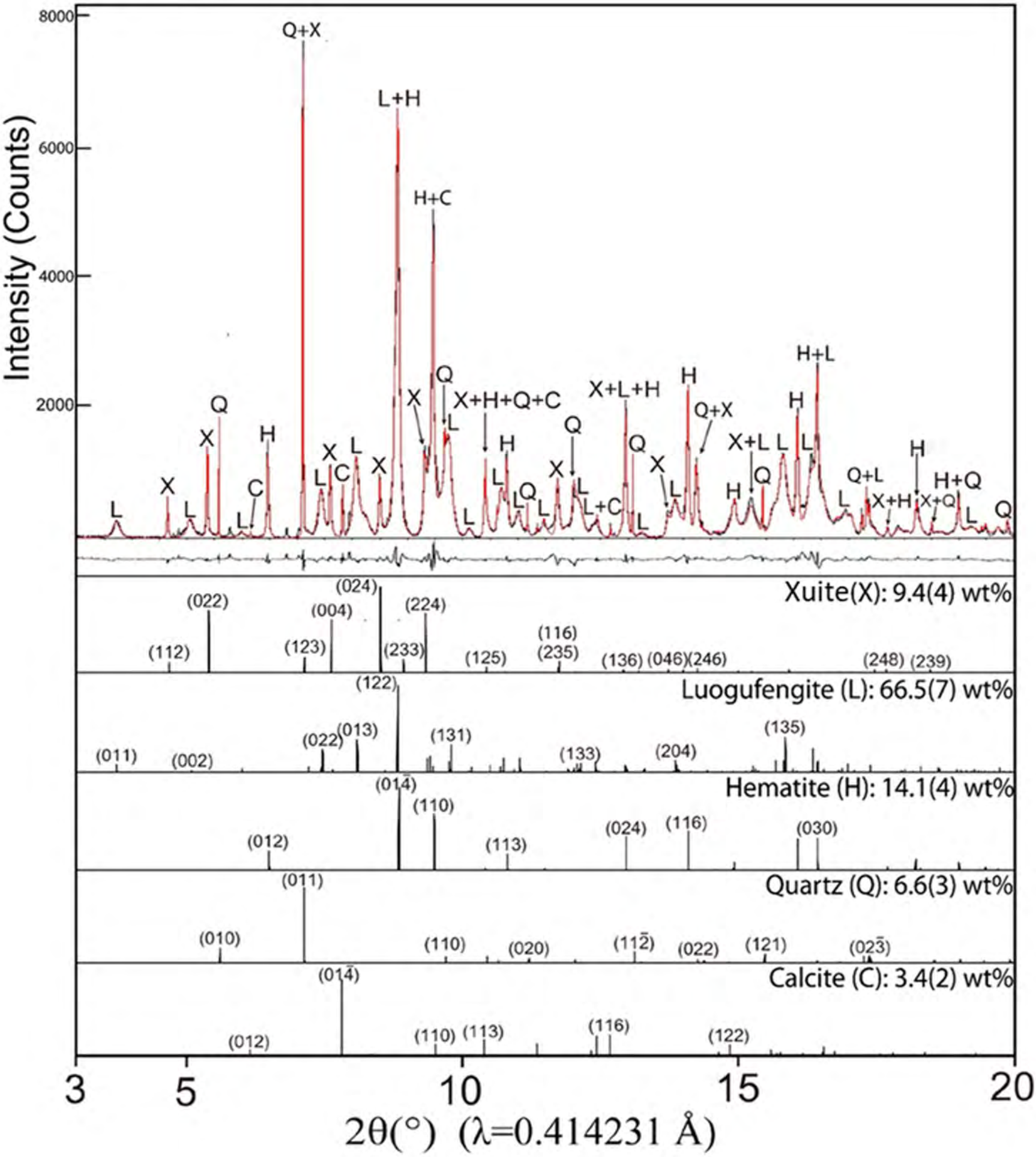
Intensity (Counts)
8000
6000
4000
2000
Q+X
L+H
H+C
Xuite(X): 9.4(4) wt%
Luogufengite (L): 66.5(7) wt%
Hematite (H): 14.1(4) wt%
Quartz (Q): 6.6(3) wt%
Calcite (C): 3.4(2) wt%
3
5
10
15
20
2θ(°) (λ=0.414231 Å)

Figure. 2

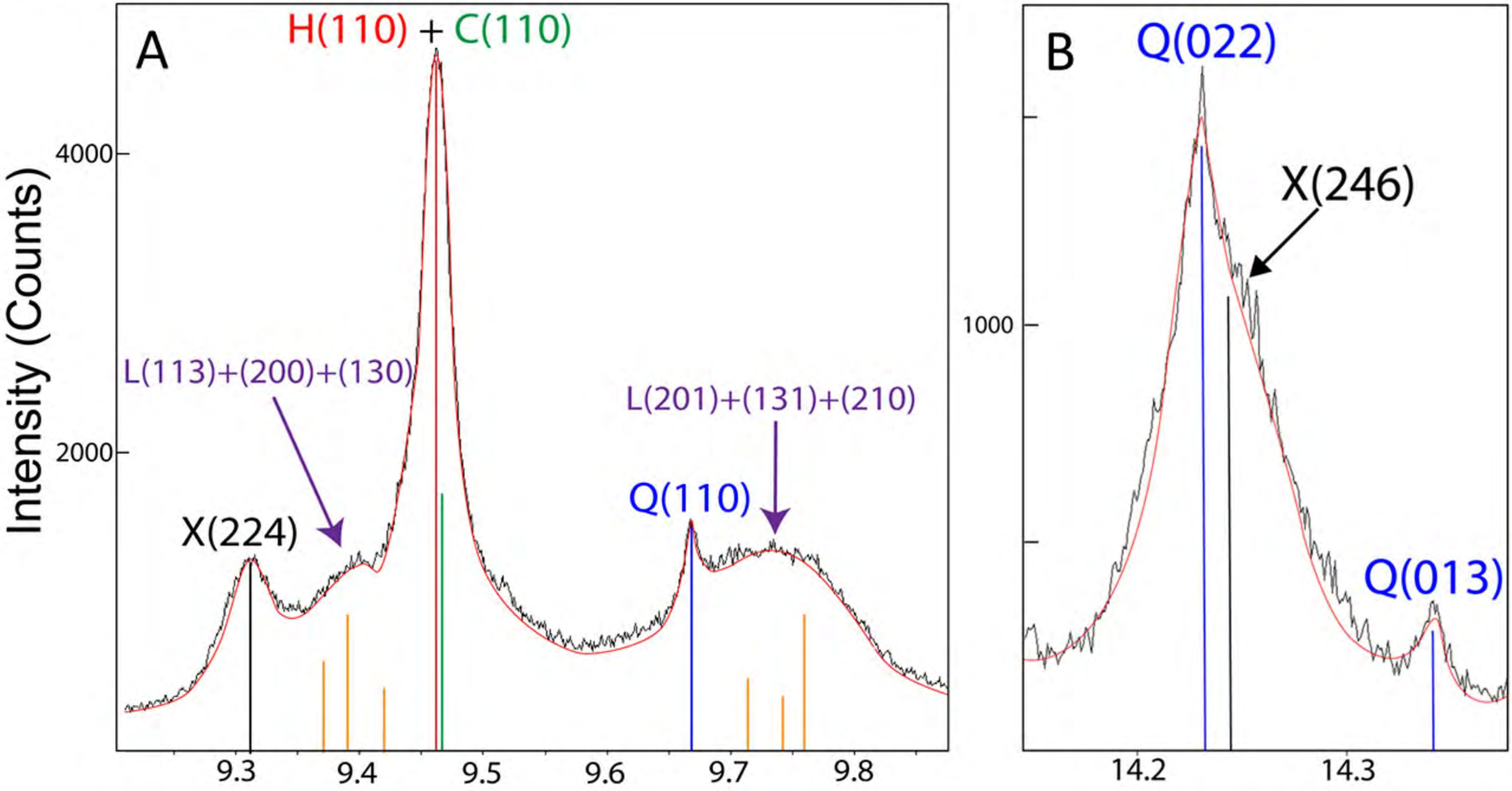
A
H(110) + C(110)
L(113)+(200)+(130)
L(201)+(131)+(210)
X(224)
Q(110)
Intensity (Counts)
4000
2000
9.3
9.4
9.5
9.6
9.7
9.8
B
Q(022)
X(246)
Q(013)
1000
14.2
14.3

Figure. 3

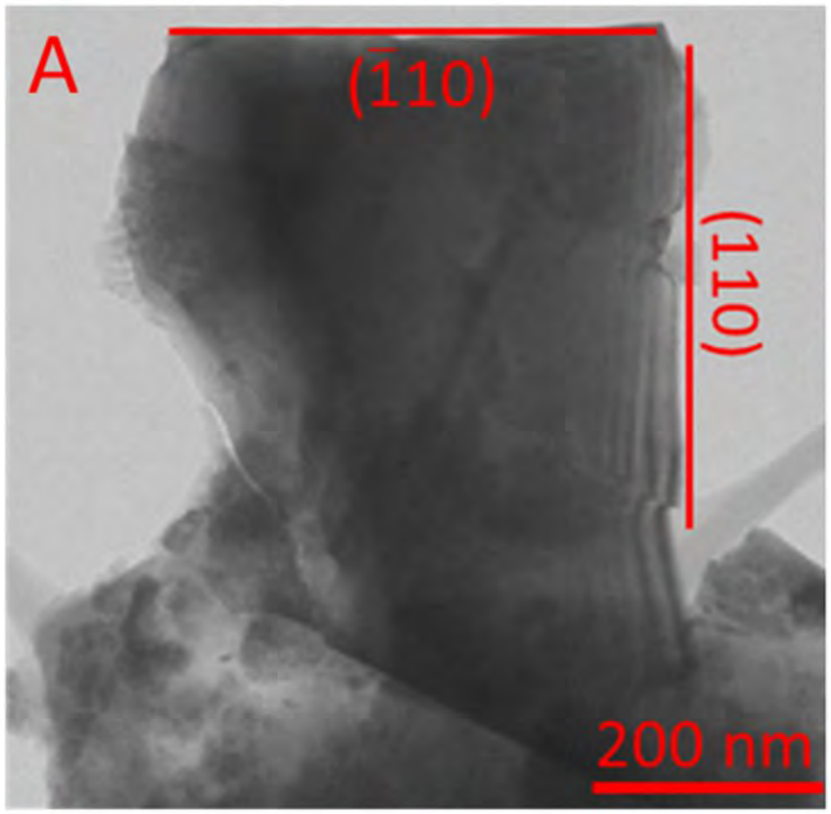
A
(1̄10)
(110)
200 nm

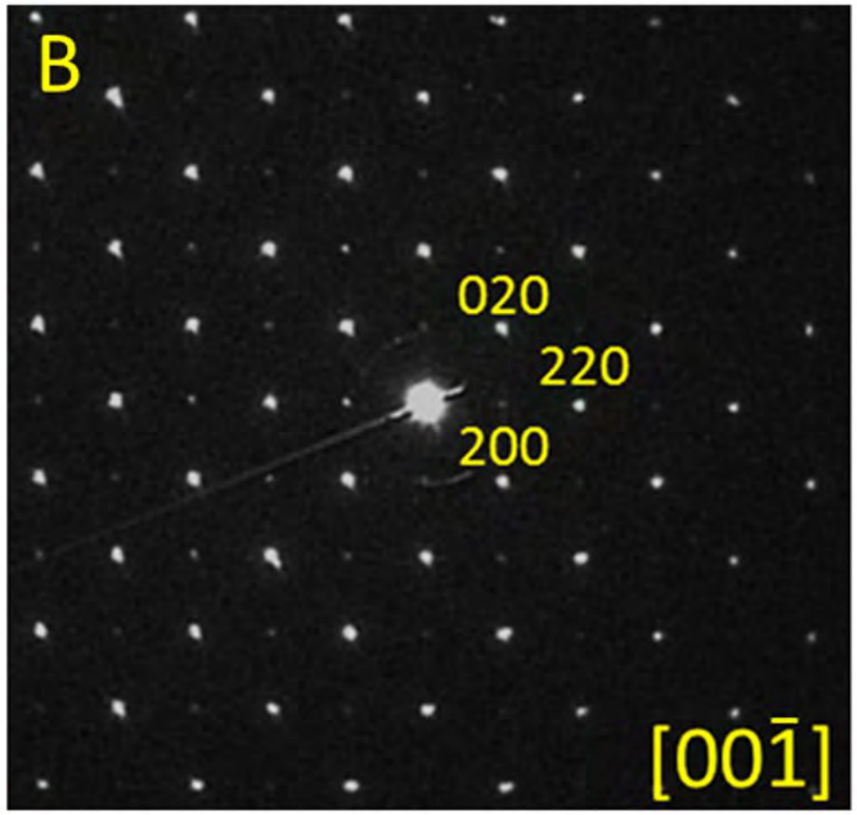
B
020
220
200
[00$\bar{1}$]

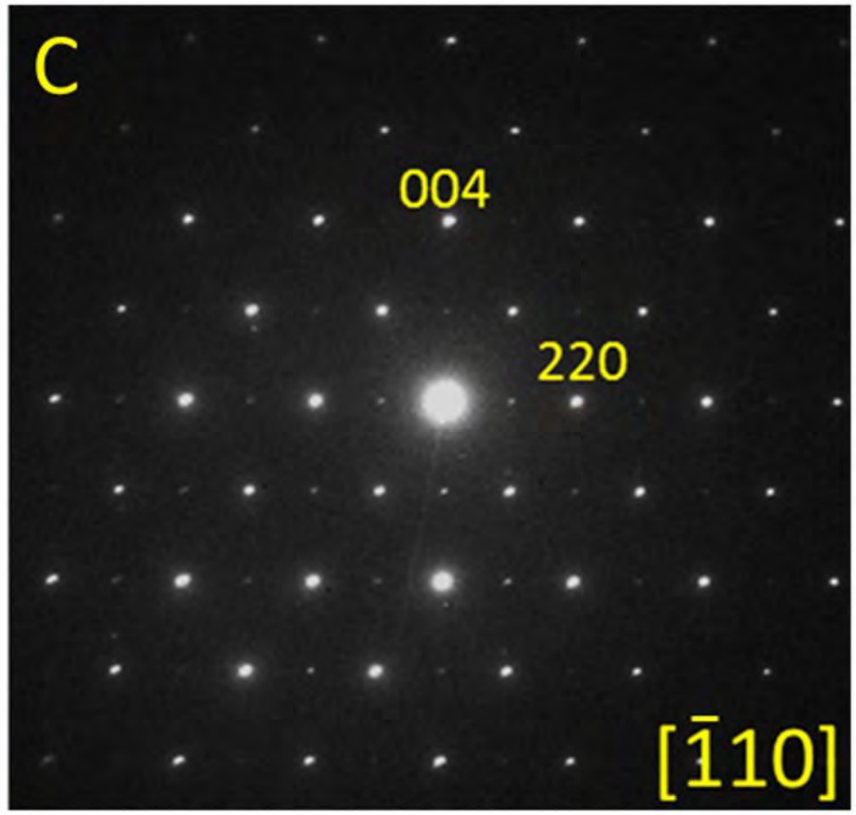
C
004
220
[$\bar{1}$10]

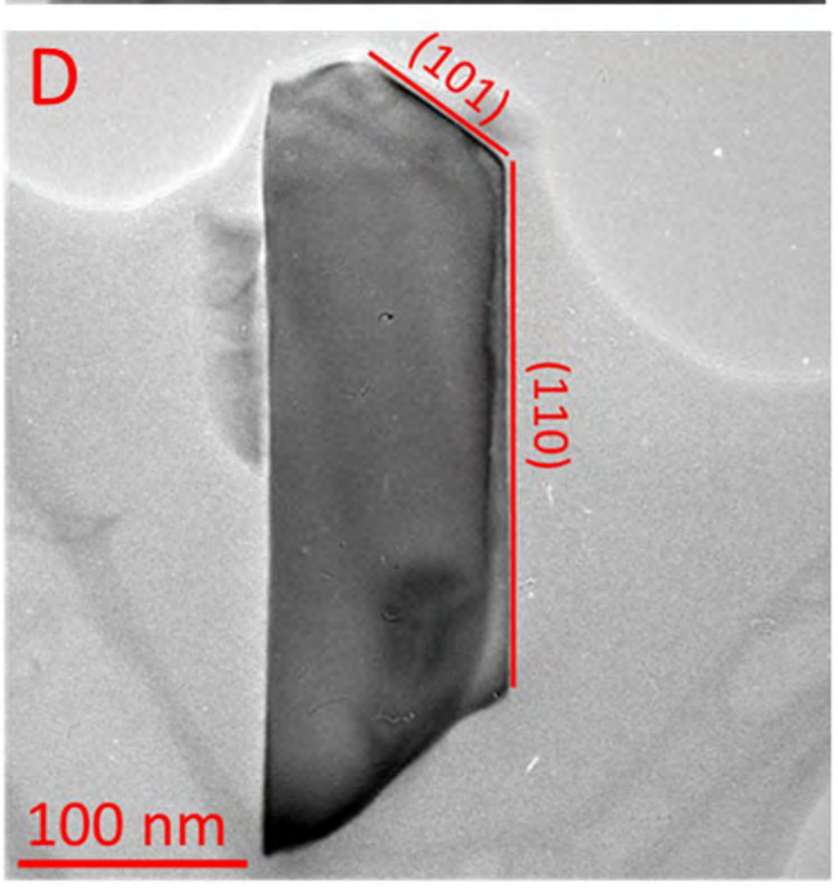
D
(101)
(110)
100 nm

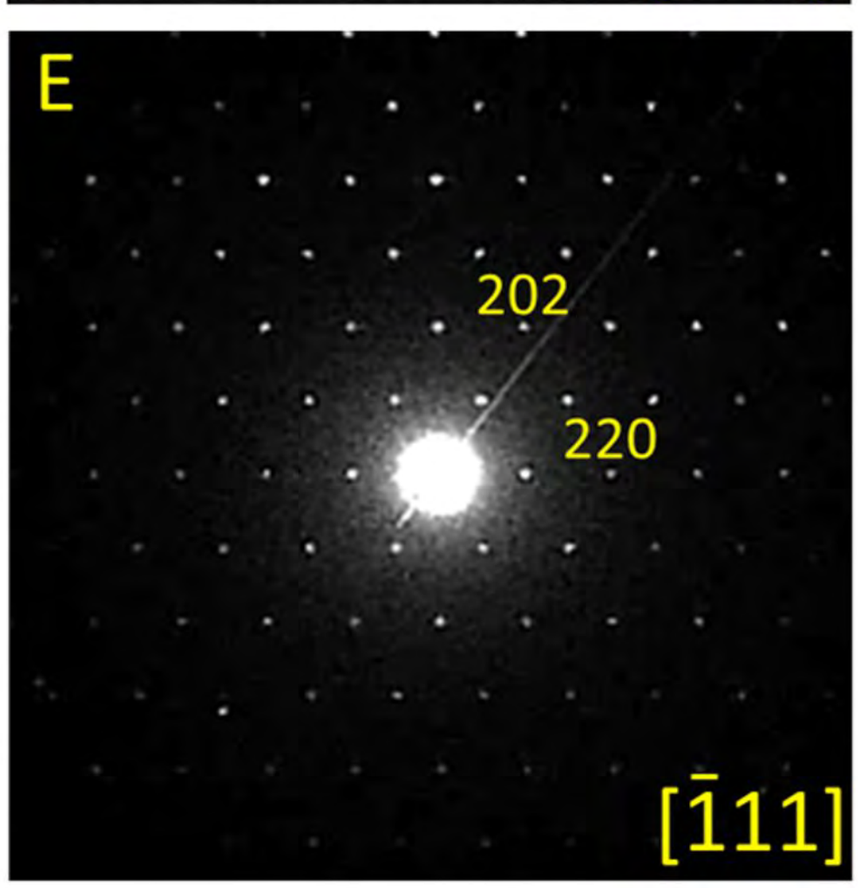
E
202
220
[$\bar{1}$11]

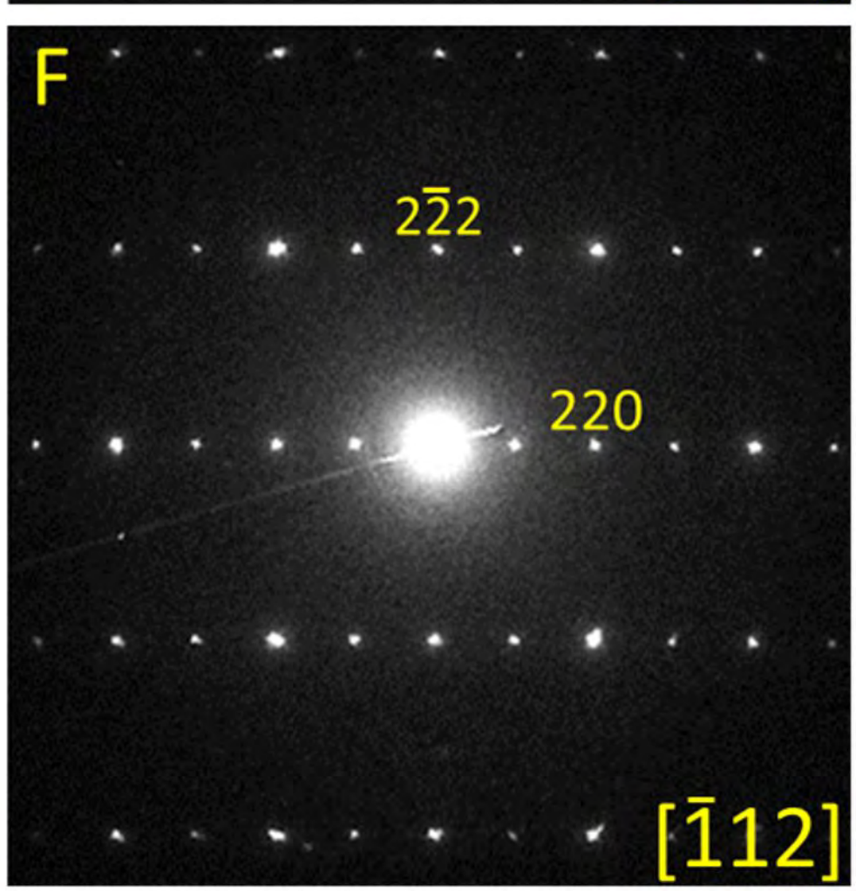
F
2$\bar{2}$2
220
[$\bar{1}$12]

Figure. 4

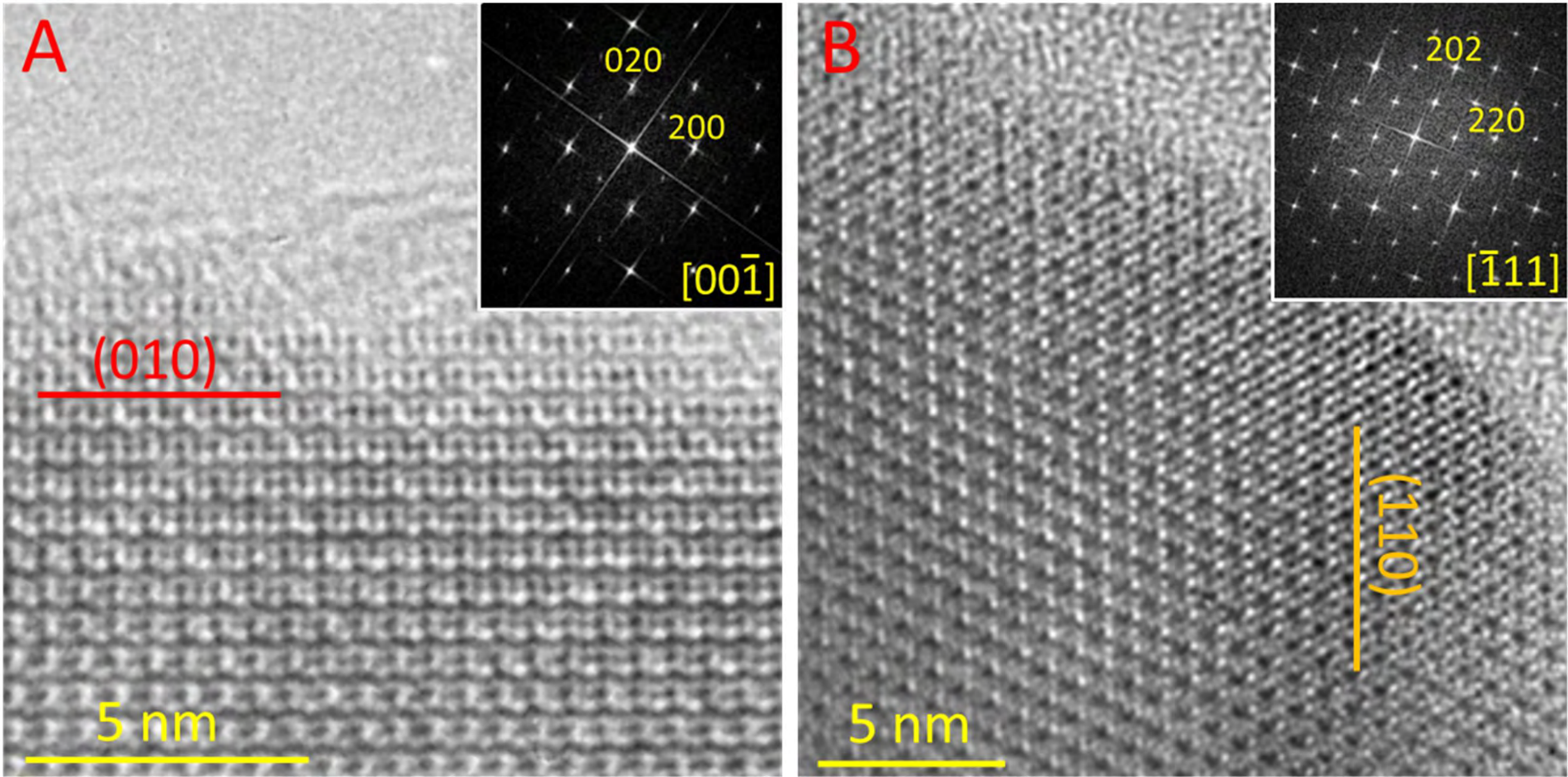

Figure. 5

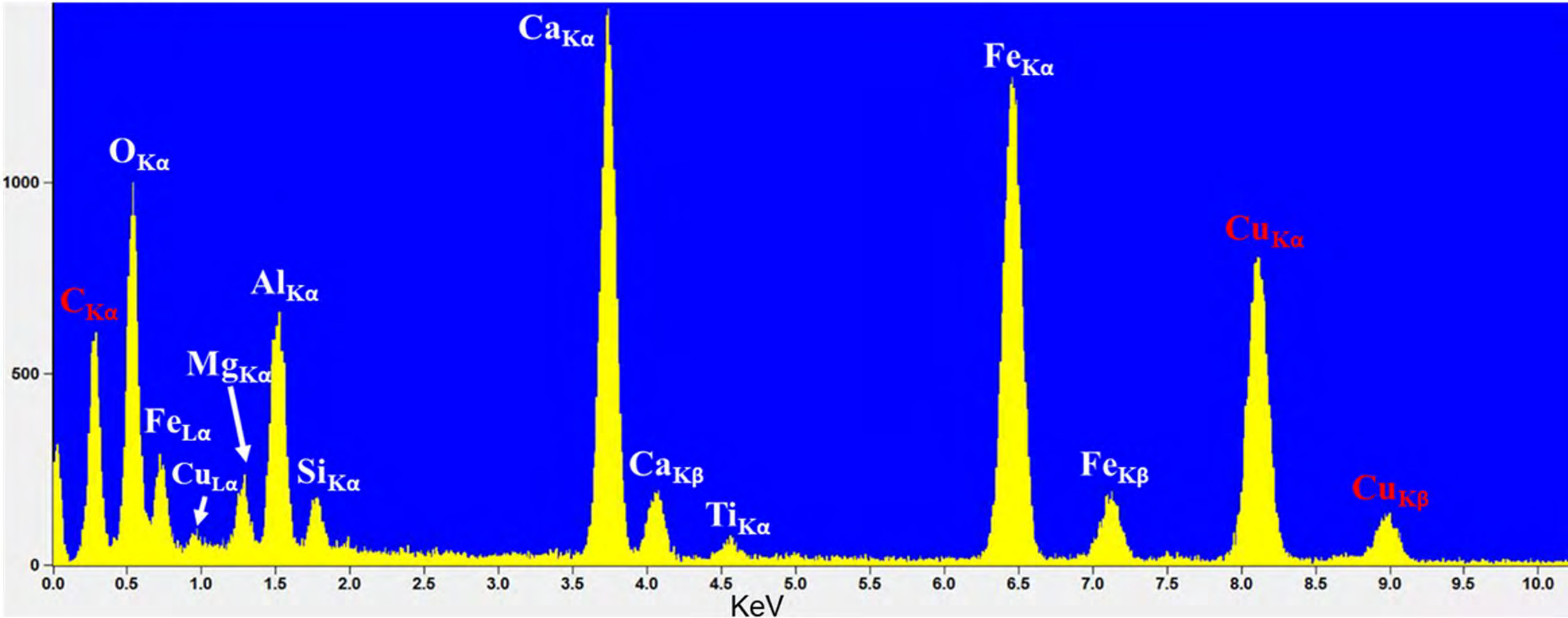
$Ca_{K\alpha}$
$Fe_{K\alpha}$
$O_{K\alpha}$
$Cu_{K\alpha}$
$C_{K\alpha}$
$Al_{K\alpha}$
$Mg_{K\alpha}$
$Fe_{L\alpha}$
$Cu_{L\alpha}$
$Si_{K\alpha}$
$Ca_{K\beta}$
$Ti_{K\alpha}$
$Fe_{K\beta}$
$Cu_{K\beta}$
1000
500
0
0.0 0.5 1.0 1.5 2.0 2.5 3.0 3.5 4.0 4.5 5.0 5.5 6.0 6.5 7.0 7.5 8.0 8.5 9.0 9.5 10.0
KeV

Figure. 6

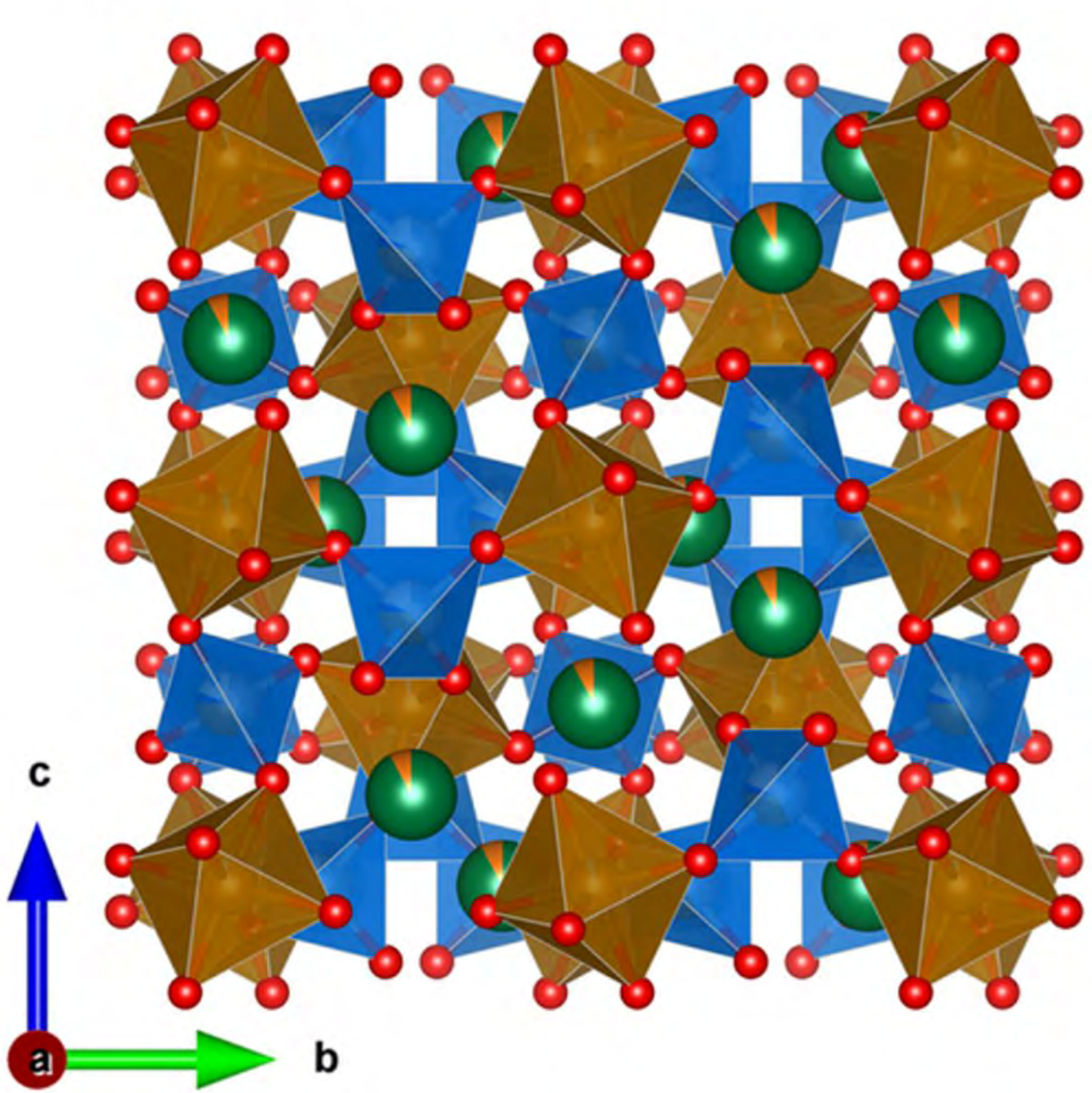

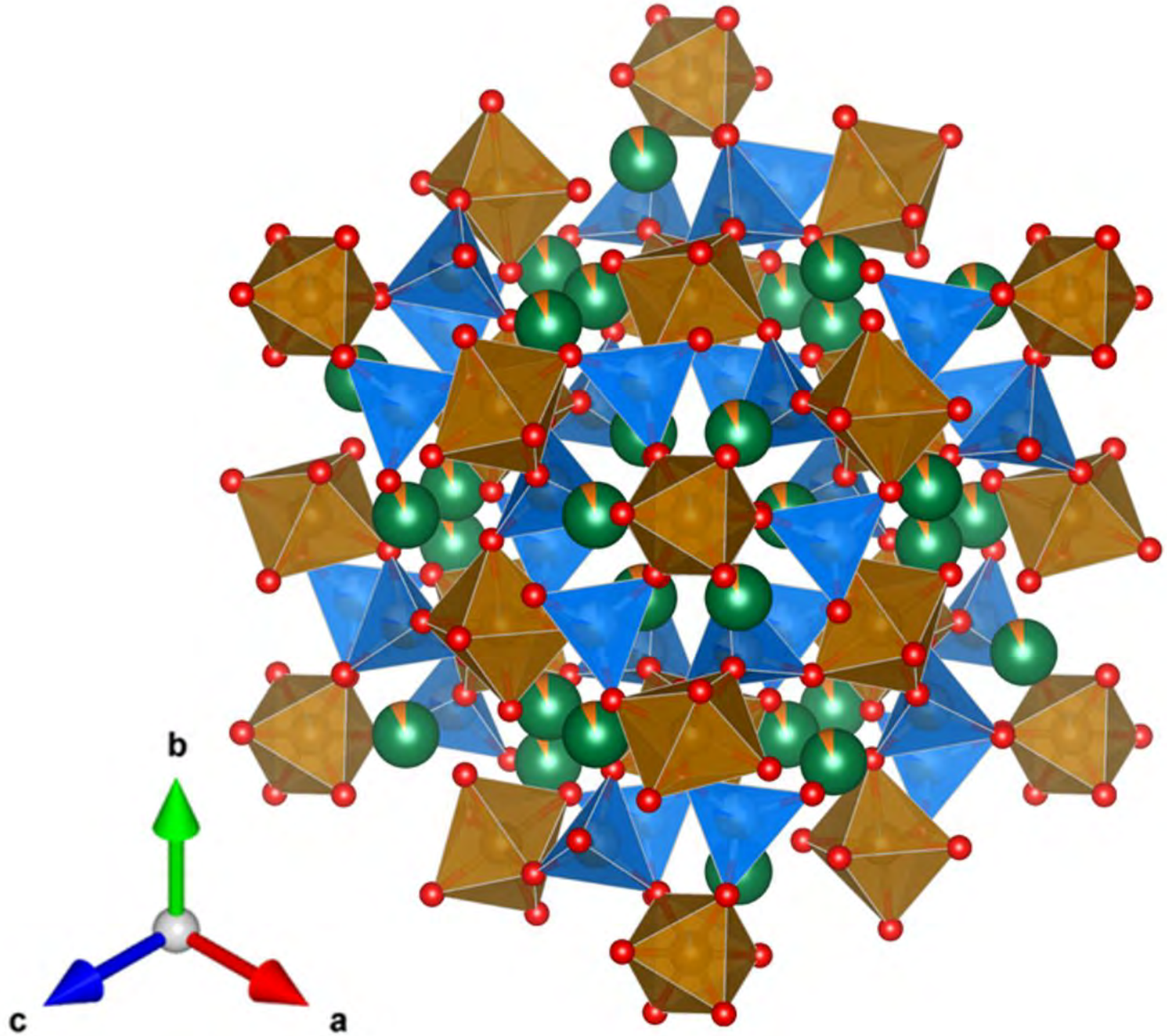

Figure. 7

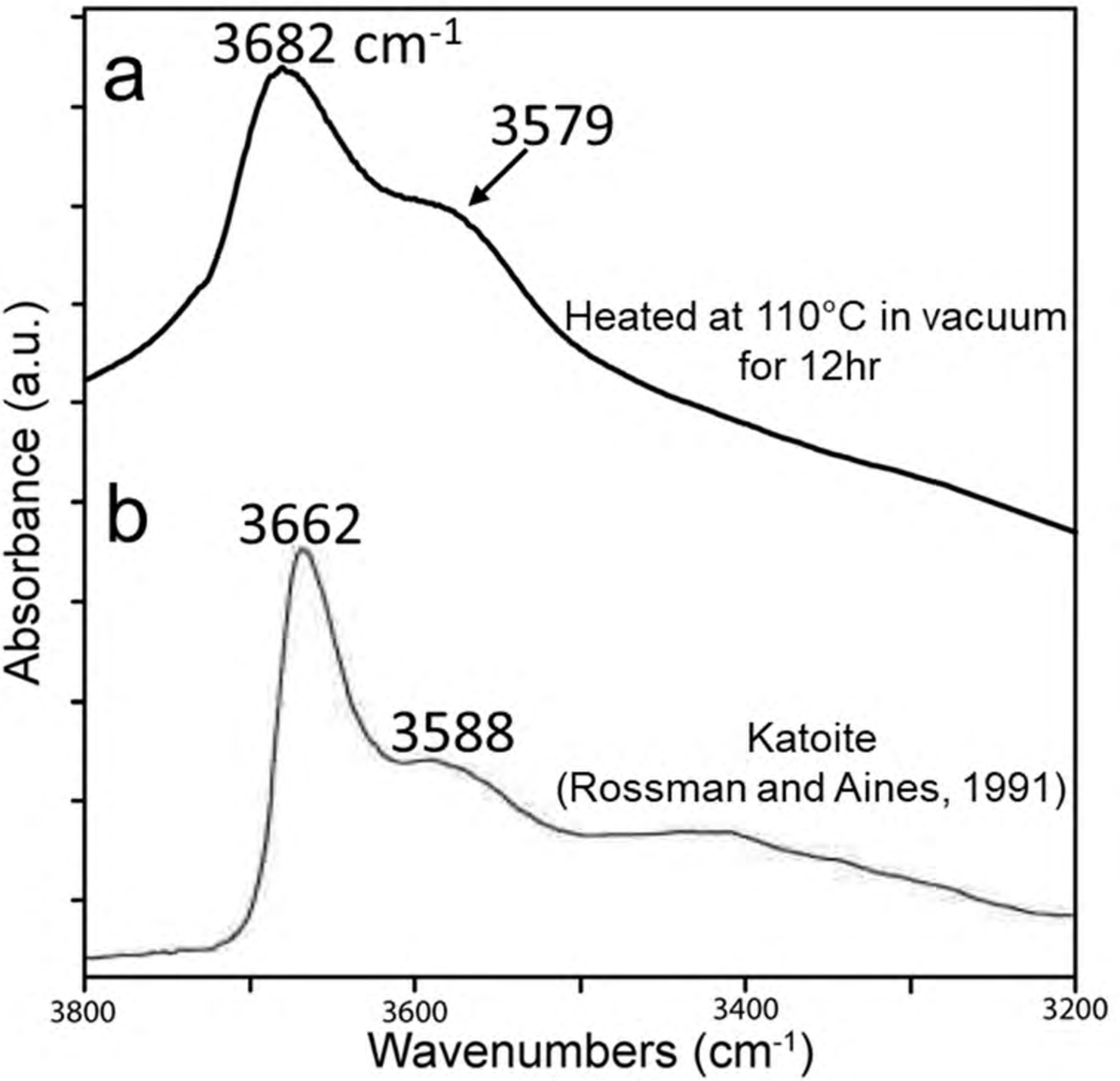
a
3682 cm-1
3579
Heated at 110°C in vacuum
for 12hr
b
3662
3588
Katoite
(Rossman and Aines, 1991)
Absorbance (a.u.)
3800
3600
3400
3200
Wavenumbers (cm-1)

Figure. 8

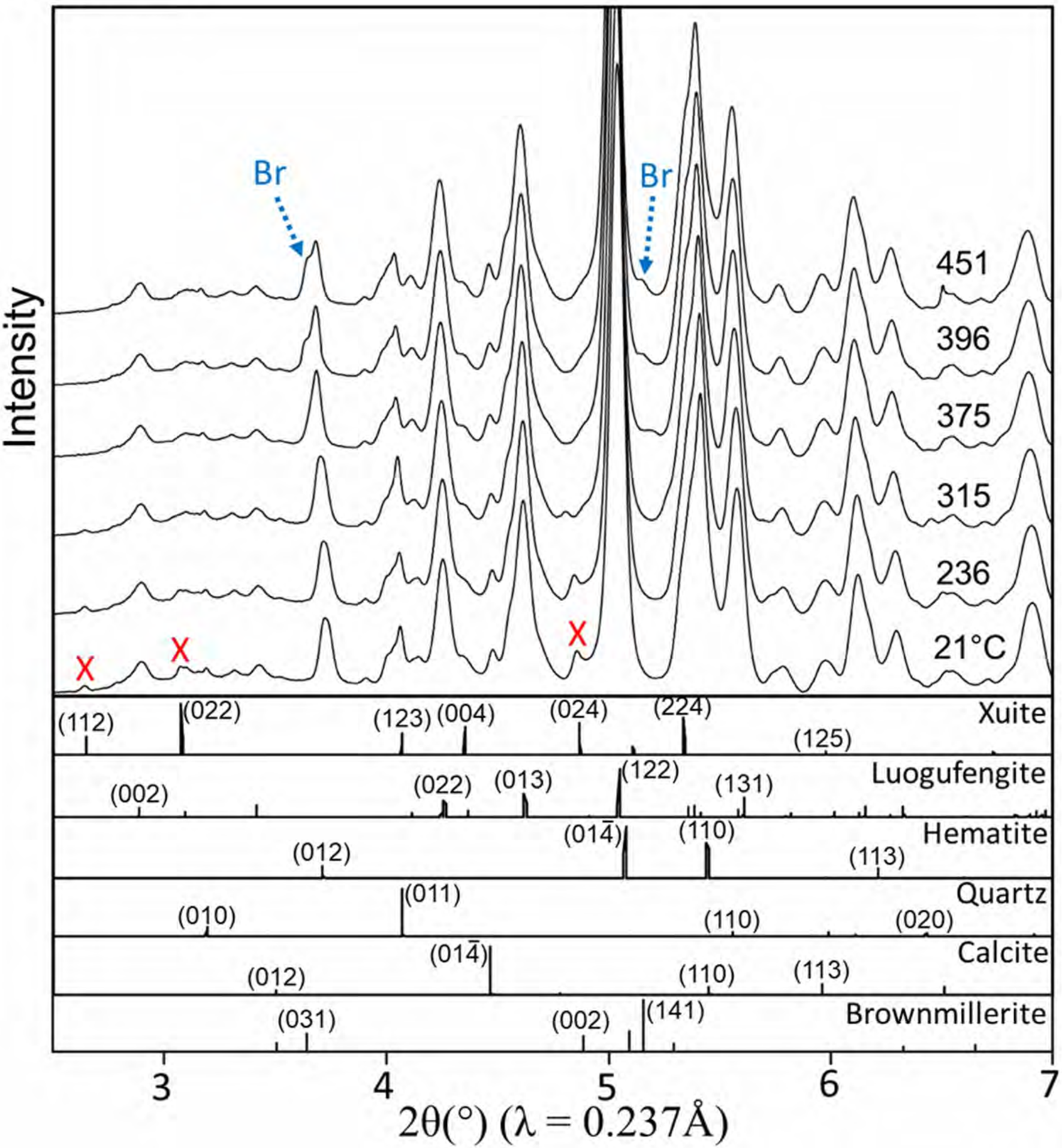
Br
Br
451
396
375
315
236
21°C
X
X
X
Intensity
(112)
(022)
(123)
(004)
(024)
(224)
(125)
Xuite
(002)
(022)
(013)
(122)
(131)
Luogufengite
(012)
(01$\bar{4}$)
(110)
(113)
Hematite
(010)
(011)
(110)
(020)
Quartz
(012)
(01$\bar{4}$)
(110)
(113)
Calcite
(031)
(002)
(141)
Brownmillerite
3
4
5
6
7
2θ(°) (λ = 0.237Å)

Figure. 9

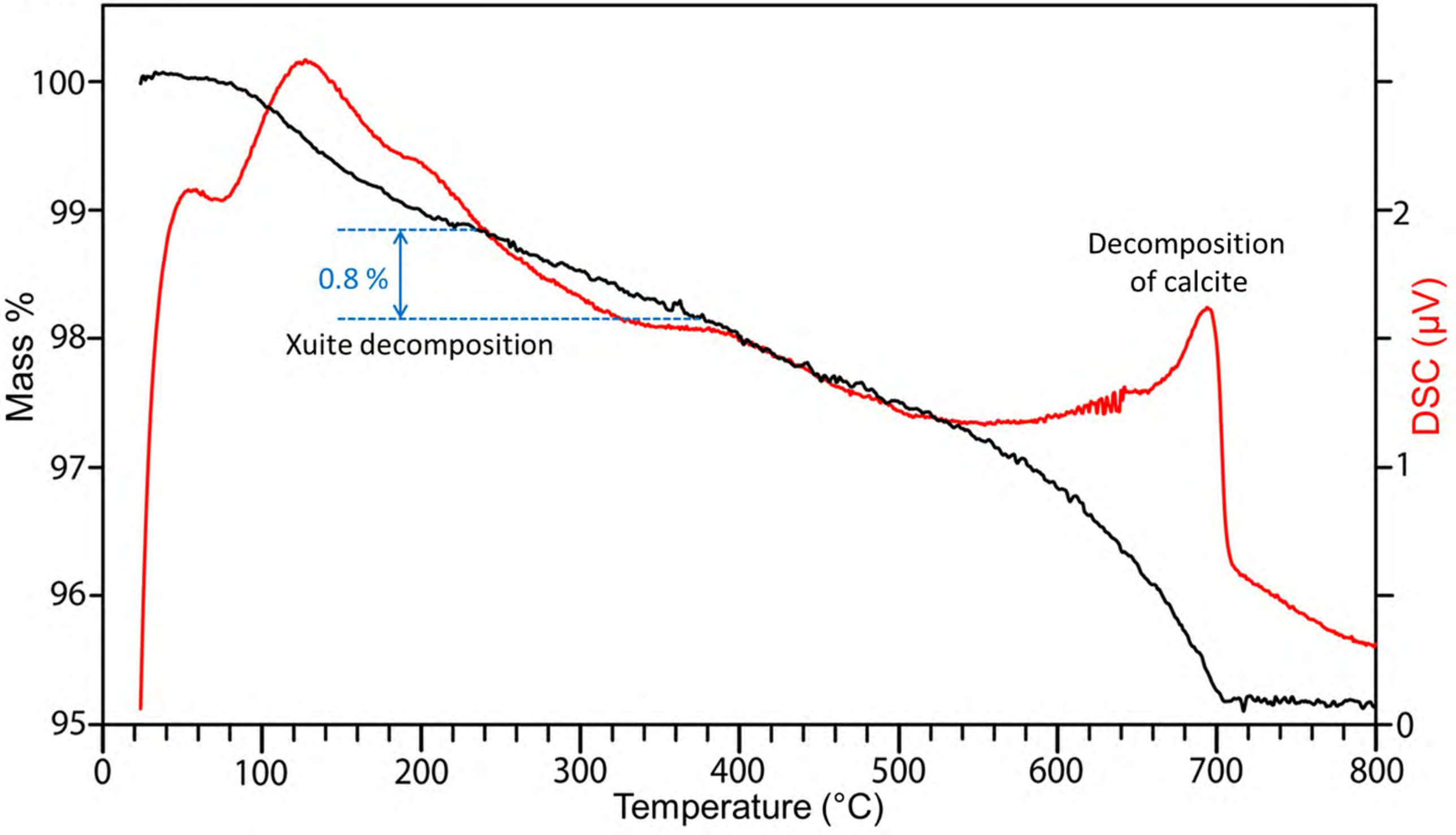
100
99
98
97
96
95
Mass %
0.8 %
Xuite decomposition
Decomposition
of calcite
2
1
0
DSC (μV)
0
100
200
300
400
500
600
700
800
Temperature (°C)